# Edge-Driven Mechanical Microplate Models of Strike-Slip Faulting in the Tibetan Plateau

# Edge-driven mechanical microplate models of strike-slip faulting in the Tibetan plateau

Meredith A. Langstaff [1] and Brendan J. Meade [1]

Received 5 November 2012; revised 11 June 2013; accepted 26 June 2013.

[1] The India-Asia collision zone accommodates the relative motion between India and Eurasia through both shortening and pervasive strike-slip faulting. To gain a mechanical understanding of how fault slip rates are driven across the Tibetan plateau, we develop a two-dimensional, linear elastic, two-stage, deformable microplate model for the upper crust based on the behavior of an idealized earthquake cycle. We use this approach to develop a suite of simple India-Asia collision zone models, differing only in boundary conditions, to determine which combination of edge forces and displacements are consistent with both the slip rate measurements along major Tibetan faults as well as the geodetically observed extrusion of crustal material toward Southeast Asia. Model predictions for the Altyn Tagh (1–14 mm/yr), Kunlun (3–10 mm/yr), Karakorum (5–12 mm/yr), and Haiyuan (3–5 mm/yr) faults are in agreement with geologically and geodetically inferred slip rates. Further, models that accurately reproduce observed slip rate gradients along the Altyn Tagh and Kunlun faults feature two critical boundary conditions: (1) oblique compressive displacement along the Himalayan range front west of the Shillong plateau, and (2) forcing in Southeast Asia. Additionally, the ratio of internal-block potency rate to the total potency rate for each microplate ranges from 28% to 79%, suggesting a hybrid view of deformation in Tibet as simultaneously localized on major faults and distributed at length scales $<$500 km.

**Citation:** Langstaff, M. A., and B. J. Meade (2013), Edge-driven mechanical microplate models of strike-slip faulting in the Tibetan plateau, *J. Geophys. Res. Solid Earth*, *118*, doi:10.1002/jgrb.50272.

## 1. Introduction

[2] The India-Asia collision zone spans as least 7 million km$^2$ and encompasses the Tibetan plateau, which stands at a mean elevation of 4 km and is dissected by large-scale strike-slip faults exceeding 1500 km in length. Modern-day convergence between the Indian and Eurasian plates is accommodated on the southern edge of the plateau by ~20 mm/yr of shortening at the Main Himalayan Thrust [*Bilham et al*., 1997; *Lavé and Avouac*, 2000; *Jouanne et al*., 2004], in the northwest at the northern boundary of the Tarim Basin by at least 14 mm/yr of convergence across the Tien Shan [*Abdrakhmatov et al*., 1996; *Thompson et al*., 2002], and in the northeast by distributed shortening and rotation [*Tapponnier et al*., 1990; *Wang et al*., 2001; *Hetzel et al*., 2004; *Loveless and Meade*, 2011]. The time-integrated effect of this shortening has been suggested as a mechanism contributing to the thickening the Tibetan crust to 60–80 km [*Chen and Molnar*, 1981; *Owens and Zandt*, 1997; *Kind et al*., 2002; *Zhang and Klemperer*, 2005].

[3] Despite crustal thickening leading to isostatically compensated surface uplift on the order of 4 km, the largest documented postcollisional deformation signals in Tibet are those associated with large-scale strike-slip faults that have accrued hundreds of kilometers of displacement. The largest, the left-lateral Altyn Tagh fault (Figure 1), extends more than 1300 km along the northern boundary of the Tibetan Plateau [*Molnar and Tapponnier*, 1975]. Post Oligocene-early Miocene cumulative offsets have been estimated between 350 and 400 km [*Yue et al*., 2001], geologically inferred slip rates range from 9 to 18 mm/yr [*Yue et al*., 2001; *Mériaux et al*., 2005; *Cowgill et al*., 2009], and geodetically inferred slip rate estimates fall between 5 and 9 mm/yr [*Bendick et al*., 2000; *Wallace et al*., 2004; *Meade*, 2007; *Loveless and Meade*, 2011]. South of the Altyn Tagh fault, estimated offsets for the east-west trending Kunlun fault (Figure 1) may be as high as 100 ± 20 km [*Fu and Awata*, 2007], consistent with the extrapolation of late Pleistocene-Holocene slip rates [11.7 ± 1.5 mm/yr, *van der Woerd et al*., 2002a] back to a possible initiation in the mid-Miocene, ~15 Ma [*Jolivet et al*., 2003]. The Red River fault (Figure 1), which trends southeast from the high plateau into south China, has accommodated between 500 and 900 km of left-lateral slip in the Oligo-Miocene; however, since then, several tens of kilometers of right-lateral slip have been documented

Additional supporting information may be found in the online version of this article.

[1]Department of Earth and Planetary Sciences, Harvard University, Cambridge, Massachusetts, USA.

Corresponding author: M. A. Langstaff, Harvard University, 20 Oxford St., Cambridge, MA 02138, USA. (mlangstaff@eps.harvard.edu)


2169-9313/13/10.1002/jgrb.50272

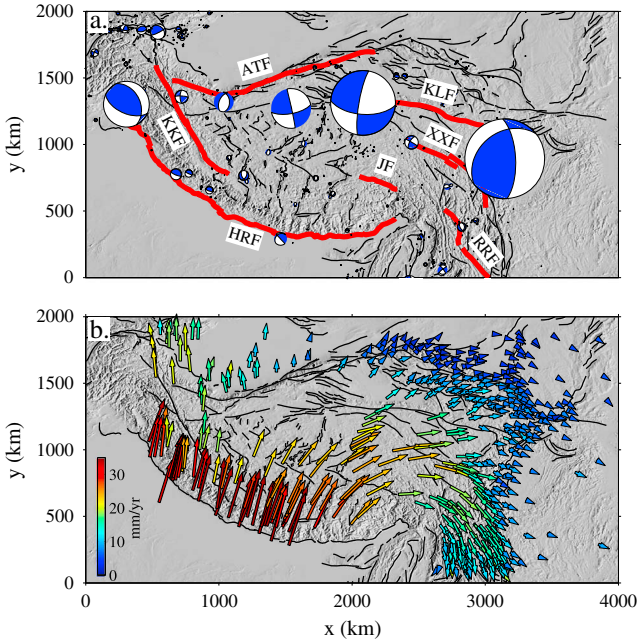


**Figure 1.** Traces of major faults, earthquake focal mechanisms ≤40 km deep (Global CMT database, compressional quadrants shaded blue, panel a), and GPS velocities *Loveless and Meade* [2011] compilation, panel b) in the greater Tibetan plateau region. Black fault traces are from *Taylor and Yin* [2009], and red traces indicate the major branches of the Altyn Tagh (ATF), Kunlun (KLF), Karakoram (KKF), Jaili (JF), Xianshuehui (XXF), and Red River (RRF) faults and the trace of the Main Frontal Thrust along the Himalayan range front (HRF). GPS velocities in a nominally Eurasian reference frame are color coded by velocity magnitude with warmer colors indicating faster velocities.

[*Leloup et al.*, 1995, 2001]. Strike-slip faulting is also present along the western edge of the Tibetan plateau, most notably along the 1200 km right-lateral Karakorum fault, which has accommodated ~250 km of displacement since ~17 Ma [*Murphy et al.*, 2000]. Karakorum slip rate estimates vary by an order of magnitude, with geologic estimates ranging from as low as 4 mm/yr [*Brown et al.*, 2002] to as high as 11 mm/yr [*Chevalier et al.*, 2005], inferences from InSAR measurements of ~1 mm/yr [*Wright et al.*, 2004], and block models constrained by GPS observations suggesting 2–4 mm /yr of right-lateral motion [*Meade*, 2007; *Loveless and Meade*, 2011].

[4] Previously proposed models for explaining the patterns of horizontal deformation across the Tibetan Plateau, and continental plate boundaries in general, have classically been divided into two categories. The first class describes plate boundary deformation as a result of the relative motion between discrete microplates [*Tapponnier et al.*, 1982; *Avouac and Tapponnier*, 1993; *Thatcher*, 2007], and serves as a foundation for block models, which integrate earthquake cycle processes with tectonic rotations to explain interseismic geodetic observations [*Chen et al.*, 2004; *Meade*, 2007; *Hilley et al.*, 2009]. The second approach approximates continental boundaries as regions undergoing continuous deformation and does not explicitly incorporate localized deformation at major faults [*England and McKenzie*, 1982; *England and Molnar*, 2005; *Flesch et al.*, 2001]. The strength of the kinematic microplate approach is the inclusion of localized deformation and earthquake cycle processes associated with major tectonic structures such as the Altyn Tagh, Kunlun, and Karakorum faults. While the second class of models neglects these discontinuities, the assumption of an effectively viscous rheology allows for the calculation of continuous strain rates and velocities everywhere in response to applied boundary conditions.

[5] Here we present a two-dimensional finite element model that unites both end-member approaches and makes testable predictions of fault slip rates. Predicting fault slip rates as a function of applied boundary conditions is distinct from the approach taken by *Peltzer and Saucier* [1996], who assumed fault slip rates and solved for a regional velocity field. This class of model incorporates both localized slip along major faults and distributed deformation within microplates with a two-dimensional two-step finite element model. Using this approach, we analyze six Tibetan plateau models to interrogate the force and displacement boundary conditions required to produce geologically and geodetically constrained slip rates along the Altyn Tagh, Kunlun, Karakoram, and Haiyuan and faults.

## 2. Dynamic Microplate Models

[6] The dynamic microplate (DM) models introduced here integrate distributed deformation within tectonic microplates with localized slip on frictionless faults (microplate boundaries). In the earth science community, various methods for dealing with partially discontinuous solutions have been developed in the context of finite element approaches [*Melosh and Raefsky*, 1981; *Dunbar and Cook*, 2003]. However, all of these approaches assume a single continuously deforming body only partially cut by faults. Finite element approaches with contact elements [e.g., *Bird*, 1999; *Chéry and Hassani*, 2005] and boundary element methods [e.g., *Crouch and Starfield*, 1983; *Bilham and Bodin*, 1992; *Olson and Cooke*, 2005; *Cooke and Dair* 2011] have also been applied to tectonic problems, but the approach here is most similar to previous iterative methods [e.g., *Kasapoglu and Toksöz*, 1983], which appear well suited to highly complex boundary geometries [*Wriggers*, 2006; *Laursen*, 2010].

[7] Our models with deformable microplates feature multiple continuously deforming bodies (Figures 2a and 2b) with displacement discontinuities at their boundaries. We solve this problem using a dual-cover finite element approach. Here dual-cover refers to the use of overlapping but separate finite element solutions. In the first stage, faults deform and fault geometries evolve in response to boundary conditions applied to a continuous global mesh encompassing all microplates (Figures 2c, 2d, and 2e). A global mesh and stiffness matrix, $\mathbf{K_G}$, is constructed for the entire model region (Figure 2c). Global displacement, $\mathbf{u_G^*}$, and force boundary conditions, $\mathbf{f_G}$, are applied to the global mesh, and global displacements, $\mathbf{u_G}$, are calculated using the finite element method, $\mathbf{u_G} = \mathbf{K_G^{-1}}\mathbf{f_G}$. This formulation assumes a simple linear elastic rheology and a discretization of the weak form of the quasi-static stress equilibrium conditions on a triangular mesh of linear plane stress finite elements. All models use a Young's modulus of 30 GPa and Poisson's ratio of 0.3. The

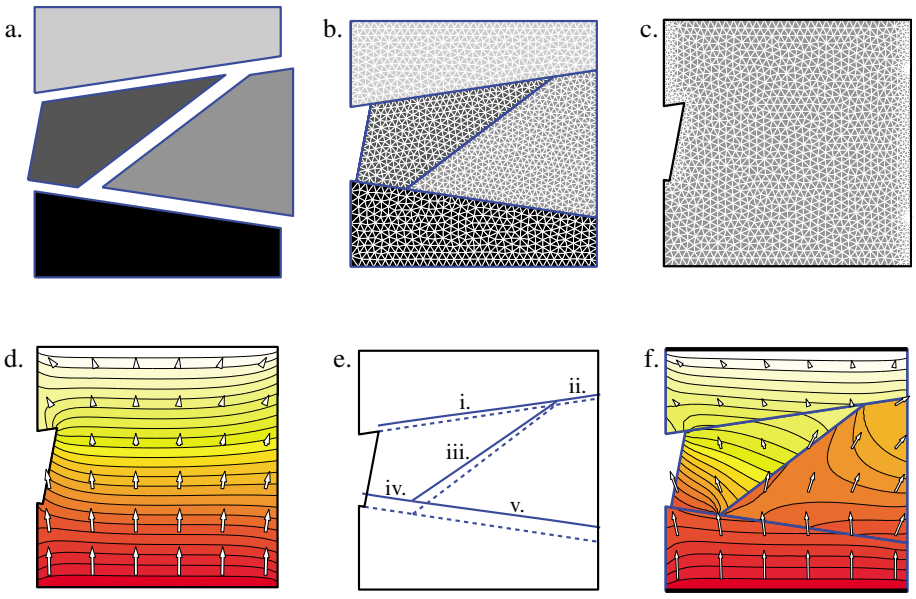


**Figure 2.** Schematic illustration of the stages in the deformable microplate model for a synthetic four block case. a) microplate geometries, b) microplate meshes, c) global mesh, d) velocity arrows and colored velocity magnitudes resulting from deformation of the global mesh due to applied boundary conditions, e) exaggerated advection of faults due to the boundary conditions applied to the global mesh, and f) velocity arrows and colored velocity magnitudes resulting from deformation of local meshes to recover fault compliance. This simple model is driven by displacement boundary conditions at the base of the model applied in the $+y$ direction, while the upper edge of the model is constrained by no slip boundary conditions. In panels d. and f., redder colors indicate large velocity magnitudes.

deflection of faults (i.e., microplate boundaries, Figure 2e) is determined from the cubic interpolation of the global displacement field (Figure 2d).

[8] In the second phase, individual microplates deform to recover geometric compliance with the deformed boundaries, thus preventing physically unrealistic gaps and overlaps between crustal microplates [e.g., *Dunbar and Cook*, 2003]. The advected microplate boundary locations calculated in phase one (Figure 2e) provide displacement boundary conditions for each microplate, and we assume that boundary nodes must always lie along the advected boundary. This compliance condition can be implemented linearly by assuming that the boundary orientation does not vary in the vicinity of individual nodes. The stiffness matrix is locally rotated at each boundary node such that the principal axes are parallel and perpendicular to the slope of the microplate boundary (supporting information). This locally straight boundary assumption means that the boundary node must be displaced a known distance normal to the fault trace, but its position in the fault-parallel direction is unknown and can vary freely, as the faults are assumed frictionless. With this assumption, we can define a local rotation matrix, $\mathbf{R_L}$, for each boundary node that introduces a coordinate system with one axis locally tangent to the fault. To ensure geometric compliance, the distance from the local node to the advected node must be constant. As a result, only the position along the boundary needs to be solved for, reducing the displacement degrees of freedom for boundary nodes to one. Displacements for each microplate are given by, $\mathbf{u_M} = \mathbf{R}\mathbf{K_M^{-1}}\mathbf{f_M}$, where $\mathbf{R}$ is a generally sparse matrix containing the local rotation submatrices, $\mathbf{R_L}$, for the boundary nodes in contact with other microplates. Thus, deformation of the fault system geometry is determined during the first FEM stage (Figure 2e), and fault slip and internal microplate deformation are determined during the second FEM stage (Figure 2f).

[9] The elastic microplate problem that we solve is connected to deformation rates by the assumption that Dirichlet boundary conditions are equal to the boundary displacements over one year. In this way, we can annualize fault slip and internal microplate stresses as slip and stressing rates. Slip rates at microplate boundaries are calculated as the difference in relative position between boundary node pairs nearest to one another and yet on opposite sides of a fault. In two-dimensions with nodes $A$ and $B$ on adjacent microplates, the differential strike-slip motion is, $s = \|\mathbf{x}_A - \mathbf{x}_B\| - \|\mathbf{x}_A + \mathbf{u}_A - \mathbf{x}_B + \mathbf{u}_B\|$, where $\mathbf{x}_A$ and $\mathbf{x}_B$ are the initial nodal positions and $\mathbf{u}_A$ and $\mathbf{u}_B$ are the displacments from the second stage of the idealized earthquake cycle model. Because of the compliance condition and the two-dimensional nature of the models presented here, only strike-slip rates are calculated and fault normal rates are zero.

[10] To demonstrate this two-stage finite element approach, we develop a simple four-block model as a representation of an idealized continental collision. Here, zero-slip displacement boundary conditions are applied at the top edge of the uppermost microplate in both the global and local steps, while at the bottom of the lowermost microplate, displacements of 50 mm/yr are applied in the positive $y$ direction. All other boundaries are stress free. Velocity discontinuities mark microplate boundaries (Figure 2e, i–v), and the sloping geometry of the faults enables the extrusion of the right-middle block in the $+x$ direction. Slip rates are highest along structures (ii) and (iii), where sinisteral slip reaches just less than 30 mm/

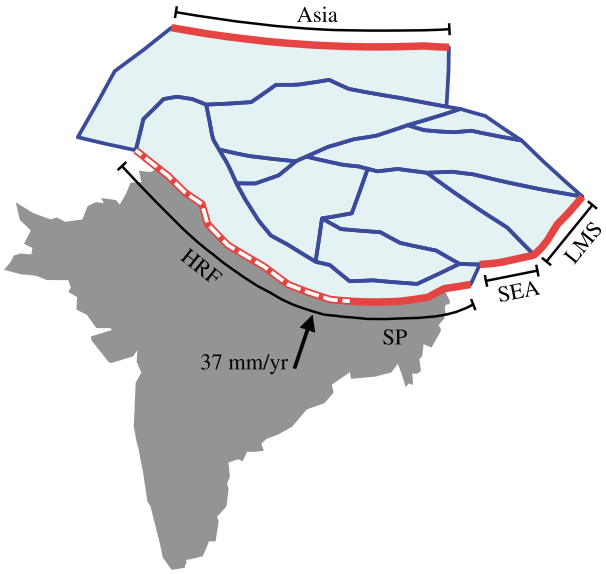


**Figure 3.** Microplate geometry and boundary conditions for DM models. Microplate boundaries are shown in blue and locations of nonstress free boundaries are shown in red. The Asia boundary is subject to a zero displacement boundary condition in all models. Convergence between India and Asia at the Himalayan range front (HRF) is assumed to be 37 mm/yr throughout [*Wang et al*., 2001] though two different spatial extents are considered. In the first, convergence is assumed to extend the entire HRF, while in the second convergence is isolated to the HRF west (dashed line) of the Shillong plateau (SP). Models with zero displacement Dirichlet conditions west of the Sichuan basin at the Longmen Shan range (LMS) are also considered, as are models with force boundary conditions in Southeast Asia (SEA).

yr and more than 27 mm/yr, respectively. All faults slip left laterally, with the exception of structure (i), which is right lateral.

## 3. DM Models of the Tibetan Plateau

### 3.1. Microplate Geometry and Boundary Conditions

[11] Model discretization of the Tibetan plateau is based on the locations of major mapped structures and locations previously hypothesized to serve as important mechanical boundaries (Figures 1a and 3). Major strike-slip faults represented include the Karakoram, Karakash, Altyn Tagh, Kunlun, Jaili, and Xianshuihe faults. Other structures such as the Ganzi, Red River, and Longmu-Gohza faults are not represented in the simplified model considered here. This fault network forms 10 microplates constituting the Tibetan plateau, Tarim Basin, and Asia (Figure 3). The Asia microplate is limited in latitudinal extent by the northern edge of the Tien Shan, which approximately marks the termination of collision-related deformation in the western half of the model domain [*Abdrakhmatov et al*., 1996]. In contrast, east of 90°E, collision-related deformation may propagate far into northeast Asia [e.g., *Calais et al*., 2003], and we consider this boundary to either be stress free or constrained by local boundary conditions described below.

[12] The northern edge of the Eurasian block represents a kinematic boundary and is modeled with zero-displacement boundary conditions (Figure 3). Three additional boundary conditions are considered in models discussed here: (1) extent of convergence and along the Himalayan range front (Dirichlet), (2) resistance at the western margin of the Sichuan basin (Dirichlet), and (3) forces acting at the southeast margin of the plateau (von Neumann). All of these are applied only at model domain edges. Each of these idealized representations of forces and displacements acting on the Tibetan plateau is motivated by a specific observation or hypothesis. Oblique (northeast-southwest) convergence between India and Asia at ~37 mm/yr is imposed as a displacement boundary condition at the Himalayan range front, consistent with geodetically observed shortening [*Wang et al*., 2001]. The spatial extent of this convergence is limited not only by the eastern and western syntaxes, but also by active shortening across the Shillong plateau ~200 km south of the Himalayan range front [*Ambraseys and Bilham*, 2003]. Thus, we consider models where the convergence along the HRF is uniform along its entire extent and those where it is limited to the ~75% of the range front west of 90°E. At the eastern margin of the plateau, the Sichuan basin has been proposed as a mechanically strong structural element preventing the eastward propagation of deformation [e.g., *Chen et al*., 2000; *Wang et al*., 2003; *Li et al*., 2006]. Southwest of the Sichuan basin, geodetic observations suggest the extrusion of upper crustal material from eastern Tibet into Southeast Asia [e.g., *Wang et al*., 2001]. Finally, the geodetically observed movement of crustal material into Southeast Asia [e.g., *Chen et al*., 2000; *Shen et al*., 2005]

**Table 1.** Predicted Slip Rates (mm/yr) and Extent of Southeastern Extrusion From Six DM Models[a]

| Model | Altyn Tagh | Karakorum | Kunlun | Xianshuihe | Jiali | Haiyuan | Extrusion |
|---|---|---|---|---|---|---|---|
| T1. HRF | 1 – 11 | (3 – 11) | (6) – 3 | (1 – 4) | (1 – 7) | (1) – 2 | N |
| T2. HRF, Fixed LMS | 1 – 11 | (3 – 11) | (6) – 2 | (3) – 6 | (1 – 4) | 0 – 6 | N |
| T3. Three-fourths HRF | 2 – 13 | (1 – 12) | (1) – 4 | 1 | (1) - 2 | 2 | N |
| T4. Three-fourths HRF, Fixed LMS | 1 – 12 | (3 – 12) | (8) – 3 | 2 – 8 | (1) – 3 | 2 – 5 | N |
| T5. HRF, SEA Force BC | 1 – 12 | (4 – 12) | 2) – 3 | (4 – 13) | (2 – 9) | 1 – 2 | N |
| T6. Three-fourths HRF, SEA Force BC | 1 – 14 | (5 – 12) | 3 – 10 | (11) – 3 | (2) – 5 | 3 – 5 | Y |

[a]Right-lateral slip rates are denoted with parentheses, while left-lateral slip rates are not. For each fault, the total variation in slip rates is given. For the case of southeast extrusion, models are deemed inconsistent with the geodetic observations only if there is no motion to the south and east along the southeastern most boundary of the plateau. In all cases, the Altyn Tagh fault is left lateral, and the Karakoram is right lateral; however, the sense of slip varies for all other major faults. Extrusion of material toward Southeast Asia is only present in models that include a local applied force along the southeastern edge of the model and convergent forcing isolated along the western three fourths of the Himalayan range front. DM model T6 (bottom) is the only one to predict and entirely left-lateral Kunlun fault.

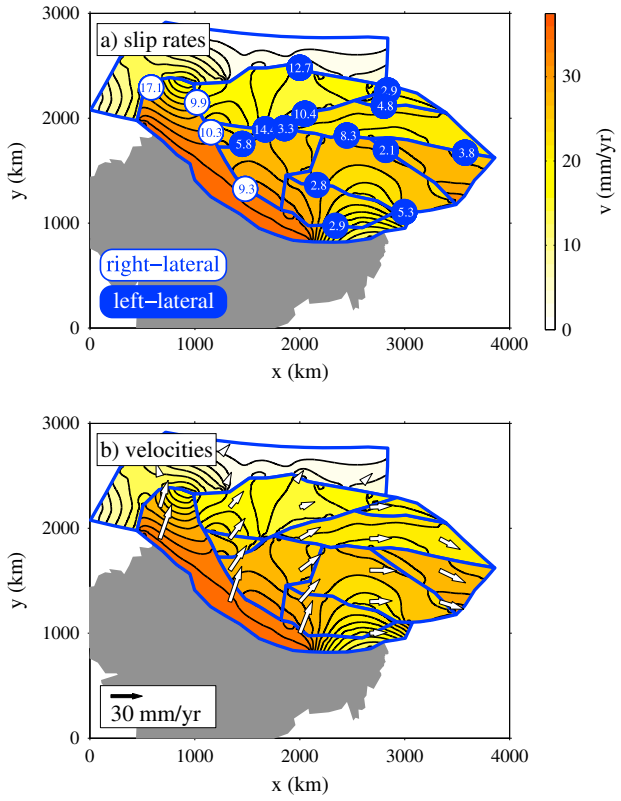


**Figure 4.** Slip rates and velocities from DM model T6 (Table 1). In all figures, microplate boundaries are shown as blue lines, and the Indian subcontinent is shaded gray. Panel a) shows fault slip rates with left-lateral rates shown as white text in blue circles and right-lateral slip rates shown as blue text in white circles. For clarity, only representative slip rates are shown here while detailed along-strike slip rate profiles are shown in Figures 5 and 6. The fastest left- and right-lateral slip rates are along the central Altyn Tagh and Karakoram faults, respectively. Color shading shows velocity magnitudes where redder colors indicate faster velocities, with maximum velocities equal to the differential motion between India and Eurasia. Velocities are continuous within each microplate, representing distributed deformation, and discontinuous at microplate boundaries, indicating fault slip. Panel b) shows velocity vectors (white arrows) superimposed over the velocity magnitude field. Velocity azimuths rotate from north-northeast to east-southeast around the eastern syntaxis.

south of the Sichuan basin has been attributed to active local forces, such as laterally constrained lower crustal flow or mantle tractions associated with rollback of the Indo-Burman slab [*Royden et al.*, 2008].

### 3.2. Sufficient Mechanisms for Strike-Slip Faulting

[13] To understand the role of edge forces in driving strike-slip faulting within the Tibetan plateau, we consider six DM models differing only in the combinations of boundary conditions described above (Table 1). Of this suite, model T6 (Table 1), with convergence displacement boundary conditions isolated to the eastern three fourths of the Himalayan range front and force boundary conditions of 1500 N/m applied along the Southeast Asia boundary (Figure 3), best explains geologically and geodetically inferred slip rates (Figures 4, 5, and 6, and Table 1). Like continuously deforming dynamic models [e.g., *England and Molnar*, 2005; *Flesch et al.*, 2001], direct comparison to geodetic observations is not yet possible for DM models due to their neglect of earthquake cycle processes which may significantly modulate GPS observations obtained during the nominally interseismic part of the seismic cycle in Tibet [e.g., *Bilham et al.*, 1997; *Chen et al.*, 2004; *Hilley et al.*, 2005; *Feldl and Bilham*, 2006; *Meade*, 2007; *Hilley et al.*, 2009]. To avoid this problem, we instead make comparisons with slip rate estimates inferred from geologic interpretations or geodetic observations interpreted with steady-state or time-dependent earthquake cycle models along specific faults.

[14] In DM model T6, extensive internal block compression is complemented by strike-slip faulting, enabling the continued northward penetration of the Pamir and Hindu Kush at the western edge of the model. Further, model T6 accommodates the extrusion of upper crustal material into Southeast Asia at the eastern edge of the model domain (Figure 4b). The eastern extrusion of the Longmen Shan block, in particular, is consistent with geodetically observed stretching in this region [*Gan et al.*, 2007]. Additionally, model T6 explains observations of entirely left-lateral slip along the Altyn Tagh (1–14 mm /yr), Kunlun (3–10 mm /yr), and Haiyuan (3–5 mm /yr) faults as well as exclusively right-lateral slip along the Karakoram fault (5–12 mm /yr, Figure 4a).

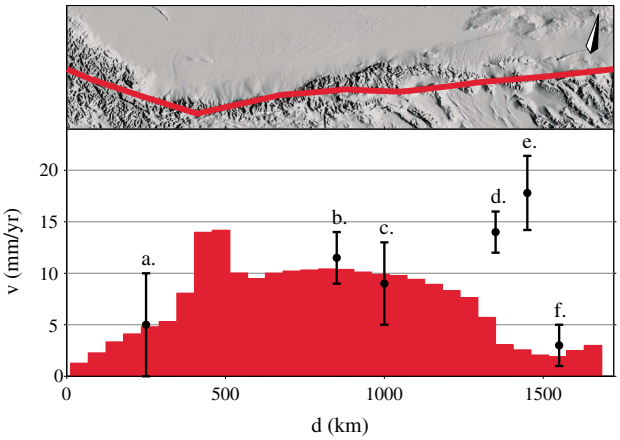


**Figure 5.** Slip rate variation along the Altyn Tagh-Karakash fault system at the northern boundary of the Tibetan plateau. The upper panel shows the rotated fault trace and topography within 200 km of the fault endpoints with the compass rose pointing north. Slip rates predicted by T6 are shown as the red fill in the lower panel with geologic and geodetic fault slip rate estimates shown as black circles with reported 1-sigma error bars. Both observations and model predictions show a peak in fault slip along the central Altyn Tagh fault reaching up to 14 mm/yr and decreasing to <5 mm/yr to both the east and west. Slip rates inferred from geologic and geodetic data are from west to east: a. 5 ± 5 *Wright et al.* [2004], b. 11.5 ± 2.5 mm/yr *Cowgill et al.* [2009], c. 9 ± 4 mm/yr *Wallace et al.* [2004], d. 14 ± 2 mm/yr *Yue et al.* [2001], e. 17.8 ± 3.6 mm/yr *Mériaux et al.* [2005], and f. 3 ± 2 mm/yr *Meade* [2007].

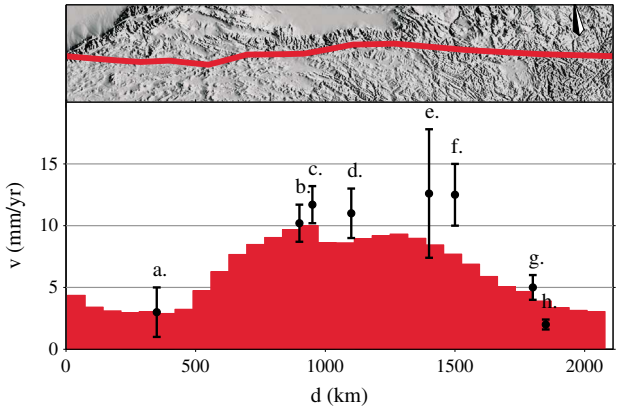


**Figure 6.** Slip rate variation along the east-west trending Kunlun fault system. The upper panel shows the rotated fault trace and topography within 200 km of the fault endpoints with the compass rose pointing north. Slip rates predicted by T6 are shown as the red fill in the lower panel with geologic and geodetic fault slip rate estimates shown as black circles with reported 1-sigma error bars. Both observations and model predictions show a peak in fault slip along the central Kunlun fault reaching up to 10 mm/yr and decreasing to <5 mm/yr to both the east and west. Slip rates inferred from geologic and geodetic data are from west to east: a. 3 ± 2 mm/yr *Bell et al*. [2011], b. 10.2 ± 1.5 mm/yr *Hilley et al*. [2005], c. 11.7 ± 1.5 mm/yr (at ~94°E) *van der Woerd et al*. [2002a], d, 11 ± 2 mm/yr *Meade* [2007], e. 12.6 ± 5.2 mm/yr (at ~99°E) *van der Woerd et al*. [2002a], f. 12.5 ± 2.5 mm/yr (at ~100.5°E) *van der Woerd et al*. [2002a], g. 5 ± 1 mm/yr at (~101.5°E) *Kirby et al*. [2007], and h. 2.0 ± 0.4 mm/yr (at ~101.75°E) *Kirby et al*. [2007].

[15] Model T6 slip rate results for the Karakoram fault (supporting information) are slightly higher than geologic and geodetic observations suggest. Slip on the Karakorum is slowest (5 mm/yr) in the northwest ~ 200 km from the intersection with the Altyn Tagh fault, but quickly increases to a maximum rate of 12 mm/yr just south of this junction. Slip rates then stabilize at ~10 mm/yr for ~600 km along strike before tapering to 7 mm/yr along the southwestern-most extent of the fault. These results are consistent with the geologic estimates of 10.7 ± 0.7 mm/yr [*Chevalier et al*., 2005] from the central and southern portions of the Karakorum but are significantly higher than geologic [4 ± 1 mm/yr, *Brown et al*., 2002] and InSAR [1 ± 3 mm/yr, *Wright et al*., 2004] observations from similar regions.

[16] Preferred model predictions for slip along the Haiyuan fault are relatively stable between 3 and 5 mm/yr. These results are consistent with geologic observations of 4.5 ± 1.1 mm/yr [*Li et al*., 2009] and InSAR estimates of 6.3 ± 2 mm/yr [*Cavalié et al*., 2008]. Block model results are in agreement with DM predictions in the eastern portion of the fault [~4 mm/yr, *Meade*, 2007], but are significantly higher than DM results on the Western portion of the fault [~9 mm/yr, *Meade*, 2007].

[17] Slip rate predictions for the Altyn Tagh fault vary by an order of magnitude along strike and are in good agreement with most geologic and geodetic measurements of slip (Figure 5). Slip rates peak at 14 mm/yr in the central western portion of the fault just south of the Tarim Basin and fall below 5 mm/yr at the western and eastern extremes of the fault trace, in agreement with InSAR observations of 5 ± 5 mm/yr in the west [*Wright et al*., 2004] and block model predictions of 3 ± 2 mm/yr in the east [*Meade*, 2007]. Slip on the central ~500 km of the fault is relatively constant at ~10 mm/yr, in accord with geologic observations of 11.5 ± 2.5 mm/yr [*Cowgill et al*., 2009] and geodetic measurements of 9 ± 4 mm/yr [*Wallace et al*., 2004] for this portion of the fault. Notably, T6 model predictions are not in agreement with geologic observations of 14 ± 2 mm/yr [*Yue et al*., 2001] and 17.8 ± 3.6 mm/yr [*Mériaux et al*., 2005] along the eastern third of the Altyn Tagh fault.

[18] One of the primary reasons DM model T6 is the preferred model for describing strike-slip faulting in Tibet is because it accurately predicts an entirely left-lateral Kunlun fault. None of the other DM models considered here correctly predict the sense of slip everywhere on this structure. DM model agreement is critical for validating the efficacy of the DM method because geologic and geodetic slip estimates for the Kunlun fault are not isolated to a single point but rather are distributed broadly along more than 1200 km of the fault's length. Model predictions peak at 10 mm/yr along the central segment of the fault and decrease below 5 mm/yr to the east and west (Figure 6). This trend is in good agreement with geologic and geodetic observations of slip, which similarly peak towards the center of the fault and are likewise <5 mm/yr at the eastern and western extremes. In particular, model slip rate gradients along the Kunlun fault are consistent with inferences from InSAR data of 3 ± 2 mm/yr on the western Manyi splay [*Bell et al*., 2011] as well as block-model inference of 11 ± 2 mm/yr [*Meade*, 2007] on the central portion of the structure. DM model T6 results also fall within range of geologic estimates from *van der Woerd et al*. [2002a] at ~99°E (12.6 ± 5.2 mm/yr), but fall just below similar calculations from ~94°E (11.7 ± 1.5 mm/yr) and ~100.5°E (12.5 ± 2.5 mm/yr) of the same study. Similarly, model predictions are consistent with estimates from *Kirby et al*. [2007] at ~101.5°E (5 ± 1 mm/yr), while the eastern-most observations at ~101.75°E (2.0 ± 0.4 mm/yr) fall slightly below model predictions.

[19] Slip rates for the Altyn Tagh and Kunlun faults are extremely sensitive to the magnitude of force applied at the SEA boundary (Figure 3 and supporting information). A fivefold increase in force boundary conditions (7500 N/m) results in a 50% increase in maximum left-lateral slip on the Altyn Tagh and an along-strike reversal in sense of slip. In these models, the eastern Altyn Tagh is heavily right lateral (maximum dexteral slip reaches >8 mm/yr). Similarly, maximum slip on the Kunlun fault is more than 500% higher than model T6 estimates (~52 mm/yr) when the SEA force boundary condition is five times higher. Further, reducing the SEA boundary condition by a factor of five (300 N/m) only slightly reduces Altyn Tagh fault slip rates, but reverses the sense of motion on the eastern Kunlun fault to ~0.5 mm/yr of right-lateral slip.

[20] Although DM model T6 is consistent with geologic and geodetic measurements for the majority of Tibetan faults and satisfies geodetically observed eastward extrusion of continental material, model predictions are inconsistent with previously inferred slip rates for the Xianshuihe and Jiali faults. DM model T6 finds low magnitude (~3 mm/yr)

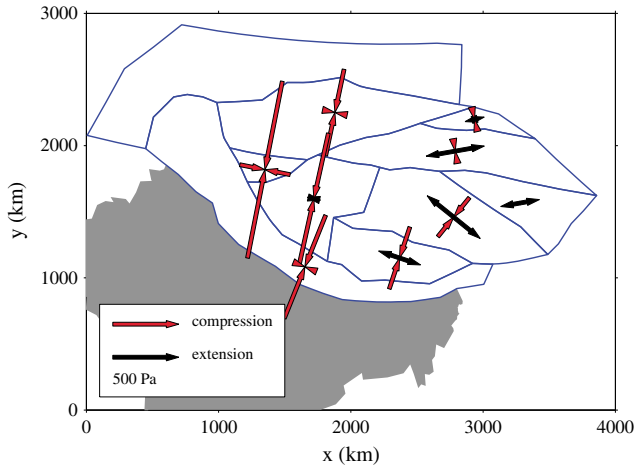


**Figure 7.** Representative principal stress orientations for model microplates, where red arrows indicate compression and black arrows indicate extension. Western microplates feature dominantly compressive principal stresses, but eastern microplates feature an extensional component.

left-lateral slip on the northern Xianshuihe fault (supporting information) decreasing along strike to 0 mm/yr in the center. Here the sense of slip reverses, and the fault becomes strongly right lateral, reaching 11 mm/yr of dextral motion at the southern extreme. All documented slip on the Xianshuihe is decisively left lateral, and while northern Xianshuihe model results are consistent with block model predictions of 3 mm/yr, block model predictions increase to 20 mm/yr of sinisteral slip for the southern portion of the fault [*Meade*, 2007]. Geologic estimates of left-lateral slip are ~15 mm/yr [*Allen et al*., 1991; *He et al*., 2006], and InSAR measurements range from 9 to 12 mm/yr [*Wang et al*., 2009].

[21] Like the Xianshuihe fault to the northwest, DM model T6 predicts (supporting information) an along-strike reversal in the sense of slip for the Jiali fault. In this case, the Jiali fault is right lateral in the western corner of the fault with a slip rate $\leq$ 2 mm/yr, but it quickly becomes left lateral, achieving sinisteral slip rates of 5 mm/yr in the east. Slip rate estimates for the Jiali fault are sparse, but model predictions do not agree with geologic estimates of 10–20 mm /yr of right lateral slip [*Armijo et al*., 1989] or block model estimates of 3–4 mm /yr of dexteral motion [*Meade*, 2007]. More realistic model representations of the complex geometry in the vicinity of the eastern syntaxis may allow more significant eastward extrusion between the Jaili and Xianshuihe faults. Despite the challenges in satisfying previously inferred slip rates on the Xianshuihe and Jiali faults, DM model T6 remains the preferred model because of the good agreement between model predictions and all other major Tibetan faults. Significantly, model T6 is the only model that satisfies geodetic and geologic observations on the densely sampled Kunlun fault and the only model that captures the eastern extrusion of Tibetan crustal material.

[22] Internal microplate principal stresses (Figure 7) calculated from model T6 are dominantly compressive through the western ~2000 km of the model, consistent with the oblique convergence displacement boundary condition on the western three fourths of the HRF. Principal stresses in the eastern half of the model domain feature an extensional component. These results are broadly consistent with the tectonic context of the region, as normal faulting in central and eastern Tibet is well documented [e.g., *Coleman and Hodges*, 1995; *Harrison et al*., 1995; *Blisniuk et al*., 2001]

## 4. Discussion

[23] While comparisons between DM model slip rate predictions and observationally constrained slip rate estimates offer a direct means of assessing model efficacy, DM models also predict pervasive nonlocalized deformation interior to microplates. This distributed deformation may be considered a coarse parameterization of faulting and folding at smaller scales or as nonbrittle deformation processes. Observationally, quantifying diffuse deformation may be challenging due to the difficulty in identifying small deformation gradients distributed over large spatial extents. However, the relative amount of total deformation associated with localized or diffuse deformation can be quantified by calculating the potency (geometric moment) rates associated with each. Localized deformation on faults has a potency rate, $P_f$, given as the product of fault area, $A$, and slip rate magnitude, $s$, such that $P_f = A|s|$. Fault potency for individual microplates is divided by two to ensure that cumulative fault potency rates are equal to the global (entire model) sum of on-fault potency [*Loveless and Meade*, 2011]. For microplate interiors, potency rates are calculated from Kostrov's formula as, $P_b = 2V\sqrt{\dot{\varepsilon}:\dot{\varepsilon}}$, where $V$ is the microplate volume, and $\dot{\varepsilon}$ is the strain rate tensor. In DM models, strain rates vary within microplates; thus, strain rates are summed over each of the triangular regions that constitute the finite element mesh. The potency partitioning ratio, $\phi = P_b/(P_b + P_f)$ [*Loveless and Meade*, 2011], quantifies the relative magnitudes of localized and diffuse deformation ranging from completely localized ($\phi = 0$) to entirely distributed ($\phi = 1$). For the microplates in DM model T6, potency partitioning ratios range from 0.28 in the microplate bounded by the Kunlun and Haiyuan faults in the northeast, to 0.79 in the block bounded by the Jaili and Xianshuihe faults in the southeast. The mean potency partitioning ratio in model T6 is 0.54 (Figure 8a). The approximate equipartitioning of localized and distributed deformation is an inherent part of the elastic rheology assumed in the model and represents a hybrid view between idealized models of rigid continental microplates bounded by major faults [e.g., *Avouac and Tapponnier*, 1993; *Shen et al*., 2005; *Thatcher*, 2007] and models of a homogenous and continuously deforming lithosphere [e.g., *England and McKenzie*, 1982; *England and Molnar*, 2005; *Holt et al*., 2000; *Flesch et al*., 2001].

[24] The geometrically and rheologically controlled microplate potency partitioning ratios can be compared against macroscale seismicity across the Tibetan plateau to assess whether or not microplates with the highest fraction of distributed internal deformation are characterized by relatively high levels of internal seismicity. We take earthquake locations from the Global CMT (www.globalcmt.org) catalog between 69° and 108°E longitude and 23°–45°N latitude with hypocenter depths shallower than 40 km. Here we consider earthquakes that are not likely to have occurred on the major faults bounding continental microplates. Thus, we filter the earthquake catalog to

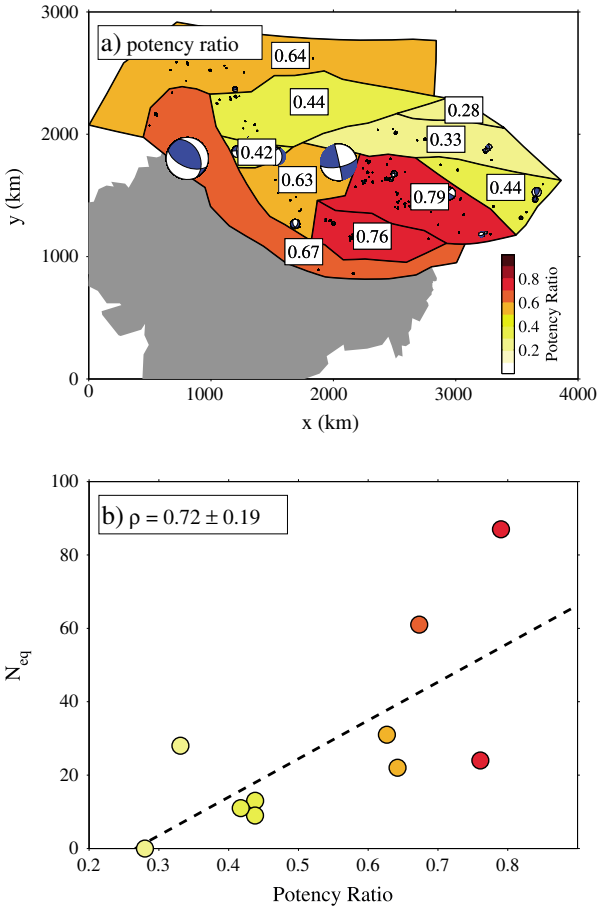


**Figure 8.** a) Potency partitioning ratios and locations of earthquakes away from major faults. Color shading gives the value of the potency partitioning ratio, $\phi$, with redder colors indicating more distributed deformation. Earthquake from the Global CMT catalog are shown with areas proportional to moment and compressional quadrants shaded blue. b) Correlation between potency partitioning ratio, $\phi$, and number of earthquakes interior to each microplate. Earthquakes are limited to those in the Global CMT catalog at depths shallower that 40 km and more than 25.1 km away from any microplate boundary. The number of earthquakes is positively correlated with high potency partitioning ratios with a Pearson correlation coefficient of 0.72 ± 0.19 (67% confidence).

eliminate all earthquakes occurring at a distance <25.1 km from model microplate boundaries (Figure 8a). Approximately 90% of the total Tibetan moment release in the historical earthquake record has occurred within 25.1 km of major faults [*Loveless and Meade*, 2011], which is within the approximate location uncertainty of CMT estimates [*Lohman and Simons*, 2005]. The Pearson correlation coefficient describing the linear relationship between the microplate potency partitioning ratios and the number of earthquakes interior to each microplate is 0.72 ± 0.19 (67% confidence, Figure 8b). This result suggests that the microplates predicted to have the greatest internal deformation (e.g., highest potency partitioning ratios) are indeed those with the highest internal seismicity rates. Because the selected earthquakes in the global CMT catalog are only those exceeding $M_W = 4.6$, this correlation is not a reflection of microscale seismicity associated with nontectonic processes. Additionally, the duration of the CMT catalog (~42 years) is much less than the typical recurrence time for large earthquakes on major faults in Tibet [e.g., *van der Woerd et al*., 2002b]. As a result, this comparison may be biased due to sampling only a small fraction of a single earthquake cycle.

[25] As described above, of the six DM models considered here, model T6 explains the slip rate observables best with two key boundary conditions: (1) convergence at 37 mm/yr along the western three fourths of the HRF west of the Shilong plateau, and (2) a southeasterly directed force of 1500 N/m acting on the SEA boundary (Figures 3 and 4). These boundary conditions are motivated by variability in geologic structure along the strike of the HRF and geodetic observations, respectively.

[26] Bounded by the Brahmaputra river to the north and west, the Shillong plateau emerges from the Indian subcontinent at 90°E and is an actively growing foreland structure. North-south oriented shortening is manifest not only geologically, but also in the occurrence of the $M_W$=8.1 Assam 1897 earthquake, which contributed to the uplift of this structure by slipping as much as 11 m on the south-southwest dipping Oldham fault at the northern edge of the plateau [*Bilham and England*, 2001]. In addition to seismic activity, geodetic data further indicate that east of 90°E deformation is partitioned, at least partially, from the HRF to the Shillong plateau bounding structures. Interseismic GPS data indicate 6.8 ± 3.8 mm/yr of differential motion between the northern edge of the Shillong plateau and the nominally stable Indian subcontinent [*Paul et al*., 2001]. Taken at face value, this convergence south of the HRF would reduce the shortening rate across the easternmost HRF by at most ~10 mm/yr, or about 30% of the overall tectonic convergence rate. While GPS data near major faults may be significantly modified throughout the earthquake cycle processes (e.g., time-dependent viscoelastic relaxation at depth), even quasi-static models of thrust faults suggest that neglecting earthquake cycle effects gives rise to minimum shortening rate estimates unless both sides of a fault are spanned by GPS stations out to several hundred kilometers [*Savage*, 1983; *Feldl and Bilham*, 2006]. Results from DM model T6, which best predicts observed Tibetan strike-slip rates and has no applied convergent displacement conditions north of Shillong plateau, are consistent with greater magnitude shortening in this region than has previously been suggested.

[27] Force boundary conditions along SEA are particularly critical for explaining observed slip rate gradients along the Kunlun fault (Table 1 and Figure 5). The observational motivation for this boundary condition is the apparent geodetic extrusion of material into Southeast Asia between the left-lateral Xianshuihe and right-lateral Jiali faults (Figure 1b). Assuming that these GPS velocities do not entirely result from transient earthquake cycle processes (e.g., large magnitude viscoelastic relaxation), the velocity at this boundary is ~15 mm/yr south-southeast, relative to stable Eurasia. The mechanism driving this deformation is less clear. Models T2 and T4 (Table 1) show that the southeastern extrusion of Tibetan crustal material is neither a necessary consequence of simple boundary conditions satisfying convergence at the HRF and confinement of Asia north of the Tien Shan, nor does it result from additional displacement

conditions such as fixing the LMS boundary. Instead, both three-fourths HRF convergence and a southeastward-directed SEA force condition are needed to successfully replicate the geodetically observed extrusion towards Burma, Laos, and Vietnam. Candidate mechanisms for local driving forces in Southeast Asia include both channelized lower crustal flow and basal tractions associated with mantle flow induced by the westward rollback of the Indo-Burman slab [*Royden et al*., 2008].

## 5. Conclusions

[28] DM models integrate the localized faulting of kinematic block models with the predictive ability of models driven exclusively by far-field boundary conditions. We suggest that DM models provide a mechanical basis for understanding along-strike variation in fault slip rates at ~1000 km length scales. Current slip rates gradients can be explained as the response of elastic upper crustal microplates deforming to accommodate the interseismic deformation of fault networks rather than resulting from lateral variations in crustal strength or thickness [e.g., *Chéry*, 2008]. Applied to two-dimensional models of strike-slip faults in the Tibetan plateau, we can predict slip rates along the Altyn Tagh-Karakash (1–14 mm /yr), and Karakoram (5–12 mm / yr) faults as well as an eastward decrease in fault slip rate along the Kunlun fault (3–10 mm /yr). Geologically and geodetically inferred slip rate gradients along the Kunlun fault may plausibly result from the application of simple displacement and force boundary conditions applied to the edges of a discontinuous elastic model. In particular, the application of convergent displacement boundary conditions along the western three fourths of the Himalayan range front and an active force dragging upper crustal material toward Southeast Asia appear as critical elements in explaining geologically and geodetically inferred fault slip rates. Although these edge-driven models explain strike-slip fault slip rates along the Altyn Tagh, Kunlun, and Karakoram faults, there is no inference that precludes a role for local gravitationally induced body forces. Many continuum models are predicated on the assumption that body forces are a driving factor in continental tectonics [*England and Molnar*, 2005; *Flesch et al*., 2001]. The efficacy of DM models with edge and body forces for explaining fault slip rates at the India-Asia boundary is a question for future work.

[29] Potency rates for DM models associated with internal block and on-fault deformation are approximately equipartitioned. This result is rheology dependent and may change significantly with the addition of nonzero coefficients of fault friction or the implementation of a more incompressible bulk crustal material. Further geologic constraints on Tibetan fault slip rates are necessary to constrain the extent of localized and distributed deformation and will be vital in determining the potential of known faults for future great earthquakes. While the DM models presented here effectively describe both geologically and geodetically inferred fault slip rates across Tibet, directly testing these models against geodetic data will require the development of representations of earthquake cycle processes. Further, DM models predict slip rate gradients along faults in the absence of mechanical heterogeneities within microplates. This result suggests that inferences of structural segmentation on faults, based exclusively on observations of along-strike slip rate variability, may be poor indicators of geometric limits to large earthquake ruptures.

## References


Abdrakhmatov, K. Y., et al. (1996), Relatively recent construction of the Tien Shan inferred from GPS measurements of present-day crustal deformation rates, *Nature*, *384*, 450–453, doi:10.1038/384450a0.

Allen, C. R., L. Zhuoli, Q. Hong, W. Xueze, Z. Huawei, and H. Weishi (1991), Field study of a highly active fault zone: the Xianshuihe fault of southwestern China, *Geol. Soc. Am. Bull.*, *103*, 1178–1199.

Ambraseys, N., and R. Bilham (2003), Reevaluated intensities for the great Assam earthquake of 12 June 1897, Shillong, India, *Bull. Seismol. Soc. Am.*, *92*(2), 655–673, doi:10.1785/0120020093.

Armijo, R., P. Tapponnier, and H. Tonglin (1989), Late Cenozoic right-lateral strike-slip faulting in southern Tibet, *J. Geophys. Res.*, *94*(B3), 2787–2838.

Avouac, J. P., and P. Tapponnier (1993), Kinematic Model of Active Deformation in Central- Asia, *Geophys. Res. Lett.*, *20*(10), 895–898.

Bell, M. A., J. R. Elliott, and B. E. Parsons (2011), Interseismic strain accumulation across the Manyi fault (Tibet) prior to the 1997 Mw 7.6 earthquake, *Geophys. Res. Lett.*, *38*, L24302, doi:10.1029/2011GL049762.

Bendick, R., R. Bilham, J. Freymueller, K. Larson, and G. H. Yin (2000), Geodetic evidence for a low slip rate in the Altyn Tagh fault system, *Nature*, *404*(6773), 69–72.

Bilham, R., and P. Bodin (1992), Slip rates on faults in the San Francisco Bay area, California, *Science*, *258*(5080), 281–284.

Bilham, R., and P. England (2001), Plauteau pop-up during the 1897 Assam earthquake, *Nature*, *410*, 806–809.

Bilham, R., et al. (1997), GPS measurements of present-day convergence across the Nepal Himalaya, *Nature*, *386*(6620), 61–64.

Bird, P. (1999), Thin-plate and thin-shell finite element programs for forward dynamic modeling of plate deformation and faulting, *Comp. Geosci.*, *25*, 383–394.

Blisniuk, P. M., B. R. Hacker, J. Glodny, L. Ratschbacher, Z. Wu, M. O. McWilliams, and A. Calvert (2001), Normal faulting in central Tibet since at least 13.5 Myr ago, *Nature*, *412*, 628–632.

Brown, E. T., R. Bendick, D. L. Bourles, V. Gaur, P. Molnar, G. M. Raisbeck, and F. Yiou (2002), Slip rates of the Karakorum fault, Ladakh, India, determined using cosmic ray exposure dating of debris flows and moraines, *J. Geophys. Res.*, *107*(B9), 2192, doi:10.1029/2000JB000100.

Calais, E., M. Vergnolle, V. San'kov, A. Lukhnev, A. Miroshnitchenko, S. Amarjargal, and J. Déverchère (2003), GPS measurements of crustal deformation in the Baikal-Mongolia area (1994-2002): implications for current kinematics of Asia, *J. Geophys. Res.*, *108*(B10), doi:10.1029/2002/JB002373.

Cavalié, O., C. Lasserre, M.-P. Doin, G. Peltzer, J. Sun, X. Xu, and Z.-K. Shen (2008), Measurement of interseismic strain across the Haiyuan fault (Gansu, China), by InSAR, *Earth Planet. Sci. Lett.*, *275*, 246–257, doi:10.1016/j.epsl.2008.07.057.

Chen, W. P., and P. Molnar (1981), Constraints on the seismic wave velocity structure beneath the Tibetan Plateau and their tectonic implications, *J. Geophys. Res.*, *86*(B7), 5937–5962, doi:10.1029/JB086iB07p05937.

Chen, Z., B. C. Burchfiel, Y. Liu, R. W. King, L. H. Royden, W. Tang, W. Wang, J. Zhao, and X. Zhang (2000), Global Positioning System measurements from eastern Tibet and their implications for India/Eurasia intercontinental deformation, *J. Geophys. Res.*, *105*(B7), 16,215–16,227.

Chen, Q. Z., J. T. Freymueller, Q. Wang, Z. Q. Yang, C. J. Xu, and J. N. Liu (2004), A deforming block model for the present-day tectonics of Tibet, *J. Geophys. Res.*, *109*, B01403, doi:10.1029/2002JB002151.

Chéry, J. (2008), Geodetic strain across the San Andreas fault reflects elastic plate thickness variations (rather than fault slip rate), *Earth Planet. Sci. Lett.*, *269*, 352–365, doi:10.1016/j.epsl.2008.01.046.

Chéry, J., and R. Hassani (2005), ADELI user's guide version 2.3: A 2D/3D finite element software for thermomechanical modeling of geological deformation, http://www.isteem.univ-montp2.fr/perso/chery/Adeli_web/doc/adeli_user_guide_3p4_3d4_v2.3.pdf

Chevalier, M. L., F. J. Ryerson, P. Tapponnier, R. C. Finkel, J. Van der Woerd, H. B. Li, and Q. Liu (2005), Slip-rate measurements on the Karakorum Fault may imply secular variations in fault motion, *Science*, *307*(5708), 411–414.

Coleman, M., and K. Hodges (1995), Evidence for Tibetan plateau uplift before 14 Myr ago from a new minimum age for east-west extension, *Nature*, *374*, 49–52.

Cooke, M. L., and L. C. Dair (2011), Simulating the recent evolution of the southern big bend of the San Andreas fault, southern California, *J. Geophys. Res.*, *116*, B04405, doi:10.1029/2010JB007835.

Cowgill, E., R. D. Gold, C. Xuanhua, W. Xiao-Feng, J. R. Arrowsmith, and J. Southon (2009), Low Quaternary slip rate reconciles geodetic and geologic rates along the Altyn Tagh fault, northwestern Tibet, *Geology*, *37*(7), 647–650, doi:10.1130/G25623A.1.

Crouch, S. L., and A. M. Starfield (1983), *Boundary Element Methods in Solid Mechanics*, Allen and Unwin, London.

Dunbar, J. A., and R. W. Cook (2003), Palinspastic reconstruction of structure maps: automated finite element approach with heterogeneous strain, *J. Struct. Geol.*, *26*, 1021–1036.

England, P., and D. McKenzie (1982), A thin viscous sheet model for continental deformation, *Geophys. J. R. Astron. Soc.*, *70*, 295–321.

England, P., and P. Molnar (2005), Late Quaternary to decadal velocity fields in Asia, *J. Geophys. Res.*, *110*, B12401, doi:10.1029/2004JB003541.

Feldl, N., and R. Bilham (2006), Great Himalayan earthquakes and the Tibetan plateau, *Nature*, *444*, 165–170, doi:10.1038/nature05199.

Flesch, L. M., A. J. Haines, and W. E. Holt (2001), Dynamics of the India-Eurasia collision zone, *J. Geophys. Res.*, *106*(B8), 16435–16460.

Fu, B., and Y. Awata (2007), Displacement and timing of left-lateral faulting in the Kunlun fault zone, northern Tibet, inferred from geologic and geomorphic features, *J. Asian Earth Sci.*, *29*, 253–265, doi:10.1016/j.jseaes.2006.03.004.

Gan, W., P. Zhang, Z.-K. Shen, Z. Niu, M. Wang, Y. Wan, D. Zhou, and J. Cheng (2007), Present-day crustal motion within the Tibetan Plateau inferred from GPS measurements, *J. Geophys. Res.*, *112*, doi:10.1029/2005JB004120.

Harrison, T. M., P. Copeland, W. S. F. Kidd, and O. M. Lovera (1995), Activation of the Nyainqentanghla Shear Zone: Implications for uplift of the southern Tibetan Plateau, *Tectonics*, *14*(3), 658–676.

He, H., H. Ran, and Y. Ikeda (2006), Uniform strike-slip rate along the Xianshuihe-Xiaojiang fault system and its implications for active tectonics in southeastern Tibet, *Acta Geol. Sin.*, *80*(3), 376–386.

Hetzel, R., M. Tao, M. Stokes, S. Niedermann, S. Ivy-Ochs, B. Gao, M. R. Strecker, and P. W. Kubik (2004), Late Pleistocene/Holocene slip rate of the Zhangye thrust (Qilian Shan, China) and implications for the active growth of the northeastern Tibetan Plateau, *Tectonics*, *23*, TC6006, doi:10.1029/2004TC001653.

Hilley, G. E., R. Bürgmann, P. Z. Zhang, and P. Molnar (2005), Bayesian inference of plastosphere viscosities near the Kunlun Fault, northern Tibet, *Geophys. Res. Lett.*, *32*, L01302, doi:10.1029/2004GL021658.

Hilley, G. E., K. Johnson, M. Wang, Z.-K. Shen, and R. Bürgmann (2009), Earthquake-cycle deformation and fault slip rates in northern Tibet, *Geology*, *37*(1), 31–34, doi:10.1130/G25157A.1.

Holt, W. E., N. Chamont-Rooke, X. Le Pichon, A. J. Haines, B. Shen-Tu, and J. Ren (2000), Velocity field in Asia inferred from Quaternary fault slip rates and Global Positioning System obeservations, *J. Geophys. Res.*, *105*(B8), 19,185–19,209.

Jolivet, M., M. Brunel, D. Seward, Z. Xu, J. Yang, J. Malavielle, F. Roger, A. Leyreloup, N. Arnaud, and C. Wu (2003), Neogene extension and volcanism in the Kunlun fault zone, northern Tibet: new constraints on the age of the Kunlun fault, *Tectonics*, *22*(5), 1052, doi:10.1029/2002TC001428.

Jouanne, F., J. L. Mugnier, J. F. Gamond, P. Le Fort, M. R. Pandley, L. Bollinger, M. Flouzat, and J. P. Avouac (2004), Current shortening across the Himalayas of Nepal, *Geophys. J. Int.*, *157*, 1–14, doi:10.1111/j.1365-246X.2004.02180.x.

Kasapoglu, K. E., and M. N. Toksöz (1983), Tectonic consequences of the collision of the Arabian and Eurasian plates: finite element models, *Tectonophysics*, *100*, 71–95.

Kind, R., et al. (2002), Seismic images of crust and upper mantle beneath Tibet: evidence for Eurasian plate subduction, *Science*, *298*, 1219, doi:10.1126/science.1078115.

Kirby, E., N. Harkins, E. Wang, X. Shi, C. Fan, and D. Burbank (2007), Slip rate gradients along the eastern Kunlun fault, *Tectonics*, *26*, TC2010, doi:10.1029/2006TC002033.

Laursen, T. A. (2010), *Computational Contact and Impact Mechanics*, Springer, Berlin.

Lavé, J., and J. P. Avouac (2000), Active folding of fluvial terraces across the Siwaliks Hills, Himalayas of central Nepal, *J. Geophys. Res.*, *105*(B3), 5735–5770.

Leloup, P. H., R. Lacassin, P. Tapponnier, U. Schärer, Z. Dalai, L. Xiaohan, Z. Liangshang, J. Shaocheng, and P. T. Trinh (1995), The Ailao Shan-Red River shear zone (Yunnan, China), Tertiary transform boundary of Indochina, *Tectonophysics*, *251*, 3–84.

Leloup, P. H., N. Arnaud, R. Lacaassin, J. R. Kienast, T. M. Harrison, T. T. Phan Trong, A. Replumaz, and P. Tapponnier (2001), New constraints on the structure, thermochronology, and timing of the Ailao Shan-Red River shear zone, SE Asia, *J. Geophys. Res.*, *106*(B4), 6683–6732, doi:10.1029/2000JB900322.

Li, S., W. D. Mooney, and J. Fan (2006), Crustal structure of mainland China from deep seismic sounding data, *Tectonophysics*, *420*, 239–252, doi:10.1016/j/tecto/2006.01.026.

Li, C., P. Zhang, J. Yin, and W. Min (2009), Late Quaternary left-lateral slip rate of the Haiyuan fault, northeastern margin of the Tibetan Plateau, *Tectonics*, *28*, TC5010, doi:10.1029/2008TC002302.

Lohman, R. B., and M. Simons (2005), Locations of selected small earthquakes in the Zagros mountains, *Geochem. Geophys. Geosyst.*, *6*, Q03001, doi:10.1029/2004GC000849.

Loveless, J. P., and B. J. Meade (2011), Partitioning of localized and diffuse deformation in the Tibetan Plateau from joint geologic and geodetic observations, *Earth Planet. Sci. Lett.*, *303*, 11–24, doi:10.1016/j.epsl.2010.12.014.

Meade, B. J. (2007), Present-day kinematics at the India-Asia collision zone, *Geology*, *35*(1), 81–84, doi:10.1130/G22924A.1.

Melosh, H. J., and A. Raefsky (1981), A simple and efficient method for introducing faults into finite element computations, *Bull. Seismol. Soc. Am.*, *71*, 1391–1400.

Mériaux, A. S., et al. (2005), The Aksay segment of the northern Altyn Tagh fault: Tectonic geomorphology, landscape evolution, and Holocene slip rate, *J. Geophys. Res.*, *110*, B04404, doi:10.1029/2004JB003210.

Molnar, P., and P. Tapponnier (1975), Cenozoic tectonics of Asia, effects of a continental collision, *Science*, *189*, 419–426.

Murphy, M. A., A. Yin, P. Kapp, T. M. Harrison, D. Lin, and G. Jinghui (2000), Southward propagation of the Karakorum fault system, southwest Tibet: timing and magnitude of slip, *Geology*, *28*(5), 451–454, doi:10.1130/00917613.

Olson, E. L., and M. L. Cooke (2005), Application of three fault growth criteria to the Puente Hills thrust system, Los Angeles, California, USA, *J. Struct. Geol.*, *27*, 1765–1777.

Owens, T. J., and G. Zandt (1997), Implications of crustal property variations for models of Tibetan Plateau evolution, *Nature*, *387*, 37–43, Geology 10, 611-616.

Paul, J., R. Bürgmann, V. K. Gaur, K. M. Larson, M. B. Ananda, S. Jade, M. Mukal, T. S. Anupama, G. Satyal, and D. Kumar (2001), The motion and active deformation of India, *Geophys. Res. Lett.*, *28*(4), doi:10.1029/2000GL011832.

Peltzer, G., and F. Saucier (1996), Present-day kinematics of Asia derived from geologic fault rates, *J. Geophys. Res.*, *101*(B12), 27,943–27,956.

Royden, L. H., B. C. Burchfiel, and R. D. Van der Hilst (2008), The geological evolution of the Tibetan Plateau, *Science*, *321*, 1054–1058.

Savage, J. C. (1983), A dislocation model of strain accumulation and release at a subduction zone, *J. Geophys. Res.*, *88*(B6), 4984–4996.

Shen, Z. K., J. N. Lu, M. Wang, R. Bürgmann (2005), Contemporary crustal deformation around the southeast borderland of the Tibetan Plateau, *J. Geophys. Res.*, *110*, B11409, doi:10.1029/2004JB003421.

Tapponnier, P., G. Peltzer, A. Y. Le Dain, R. Armijo, and P. Cobbold (1982), Propagating extrusion tectonics in Asia: new insights from simple experiments with plasticine, *Geology*, *10*(12), 611–616.

Tapponnier, P., et al. (1990), Active thrusting and folding in the Qilian Shan, and decoupling between upper crust and mantle in northeastern Tibet, *Earth Planet. Sci. Lett.*, *97*, 382–403.

Taylor, M., and A. Yin (2009), Active structures of the Himalayan-Tibetan orogen and their relationships to earthquake distribution, contemporary strain field, and Cenozoic volcanism, *Geosphere*, *5*(3), 199–214, doi:10.1130/GES00217.1.

Thatcher, W. (2007), Microplate model for the present-day deformation of Tibet, *J. Geophys. Res.*, *112*, B01401, doi:10.1029/2005JB004244.

Thompson, S. C., R. J. Weldon, C. M. Rubin, K. Abdrakhmatov, P. Molnar, and G. W. Berger (2002), Late quaternary slip rates across the central Tien Shan, Kyrgyzstan, central Asia, *J. Geophys. Res.*, *107*(B9), 2203, doi:10.1029/2001JB000596.

Van der Woerd, J., P. Tapponnier, F. Ryerson, A. Mériaux, B. Meyer, Y. Gaudemer, R. Finkel, M. Caffee, Z. Guoguang, and X. Zhiqin (2002a), Uniform postglacial slip-rate along the central 600 km of the Kunlun Fault (Tibet), from 26Al, 10Be, and 14C dating of riser offsets, and climatic origin of the regional morphology, *Geophys. J. Int.*, *148*(3), 356–388, doi:10.1046/j.1365-246x.2002.01556.x.

Van der Woerd, J., A. Mériaux, Y. Klinger, F. J. Ryerson, Y. Daudemer, and P. Tapponnier (2002b), The 14 November 2001, Mw = 7.8 Kokoxili earthquake in northern Tibet (Qinghai Province, China), *Seismo. Res. Lett.*, *73*(2), 125–135.

Wallace, K., G. H. Yin, and R. Bilham (2004), Inescapable slow slip on the Altyn Tagh fault, *Geophys. Res. Lett.*, *31*, L06613, doi:10.1029/2004GL021014.

Wang, Q., et al. (2001), Present-day crustal deformation in China constrained by global positioning system measurements, *Science*, *294*(5542), 574–577.

Wang, C.-Y., W. W. Chan, and W. D. Mooney (2003), Three dimension velocity structure of crust and upper mantle in southwestern China and its tectonic implications, *J. Geophys. Res.*, *108*(B9), 2442, doi:10.1029/2002JB001973.

Wang, H., T. J. Wright, and J. Biggs (2009), Interseismic slip rate of the northwestern Xianshuihe fault from InSAR data, *Geophys. Res. Lett.*, *36*, L03302, doi:10.1029/2008GL036560.

Wriggers, P. (2006), *Computational Contact Mechanics*, *2*nd ed. Springer, Berlin.

Wright, T. J., B. Parsons, P. C. England, and E. J. Fielding (2004), InSAR observations of low slip rates on the major faults of western Tibet, *Science*, *305*, 236–239.

Yue, Y., B. D. Ritts, and S. A. Graham (2001), Initiation and long-term slip history of the Altyn Tagh fault, *Int. Geol. Rev.*, *43*, 1087–1093.

Zhang, Z., and S. L. Klemperer (2005), West-east variation in crustal thickness in northern Lhasa block, central Tibet, from deep seismic sounding data, *J. Geophys. Res.*, *110*, B09403, doi:10.1029/2004JB003139.